Observation of negative longitudinal magnetoresistance in the type-II Dirac semimetal $PtSe_2$

Zhaoguo Li,* Yong Zeng, Jicheng Zhang, Minjie Zhou, and Weidong Wu†
Research Center of Laser Fusion, China Academy of Engineering Physics, Mianyang 621900, China

(Received 1 January 2018; revised manuscript received 18 March 2018; published 29 October 2018)

The negative longitudinal magnetoresistance (NLMR) was observed in type-II Dirac semimetal $PtSe_2$ ultrathin microflakes. The NLMR disappeared when the magnetic field direction deviates from that of the electric field, or when the temperature is above a critical value, even when the Fermi level is away from Dirac point. The physical mechanism behind NLMR may relate to the chiral anomaly of Dirac fermions or the nontopological effect in $PtSe_2$ material.

DOI: 10.1103/PhysRevB.98.165441

I. INTRODUCTION

Weyl semimetal is a three-dimensional (3D) topological state of matter, in which the conduction and valence energy bands touch at a finite number of nodes [1]. The nodes always arise in pairs and locate at the different k points. In each pair the Weyl fermions carry opposite chirality and linear dispersion. The Weyl nodes are robust against perturbations because the Weyl Hamiltonian uses all three Pauli matrices, they cannot be gapped unless they mix with a fermion of opposite chirality. However, the paired Weyl nodes are degenerate while the inversion and time symmetries are preserved, and in such a case the system is characterized by a Dirac Hamiltonian (dubbed Dirac semimetal) [2]. The Dirac points are not robust against perturbations because there are additional fourfold Dirac matrices that can be used to open a gap at the Dirac point. The Weyl and Dirac semimetals can be classified into type-I and type-II [3], depending on whether the Lorentz invariance is preserved or not. For type-I topological semimetals, respecting Lorentz symmetry, the massless Dirac fermions with linear dispersions are expected at the Weyl or Dirac points. In contrast, the type-II Weyl and Dirac fermions emerge at the topologically protected touching points of the electron and hole pockets, and they present strongly tilted Dirac cones along certain momentum directions, thereby breaking the Lorentz symmetry. These Lorentz-violating Weyl and Dirac fermions can give rise to many novel physical phenomena, such as the anisotropic chiral anomaly [4], the anomalous Klein tunneling [5], and the unusual magnetoresponse [6,7], etc.

Platinum diselenide ($PtSe_2$) is a candidate for a type-II Dirac semimetal, in which the strongly tilted Dirac cones emerge at the boundary between electron and hole pockets and distribute along the k_z axis in the Brillouin zone [8]. The type-II Dirac fermions are further experimentally confirmed in $PtSe_2$ by using angle-resolved photoemission spectroscopy [9,10]. As a new topological semimetal, the exotic transport properties of $PtSe_2$ are rarely investigated [11–13]. Furthermore, the few-atomic layers $PtSe_2$ has aroused great interest for nanoscale electronic and photoelectronic applications [14–20]. Therefore, the electrical transport study of $PtSe_2$ microflakes is of great research significance not only for fundamental physics but also for future electronic applications.

In this work paper, we report on the magnetotransport properties of thin $PtSe_2$ microflakes by changing the angle θ between the magnetic field and electric field in the sample plane. The negative magnetoresistance (MR) is observed with a $\boldsymbol{B}\|\boldsymbol{E}$ condition at low temperatures. This negative MR is actually sensitive to the angle, temperature and back gate voltage. The physical mechanism behind these observations is further discussed. Our work reveals an exotic transport phenomenon in $PtSe_2$ microflakes, which may be useful for future applications.

II. EXPERIMENTAL

The $PtSe_2$ single crystals are purchased from HQ Graphene, the Netherlands. Figure 1(a) shows the x-ray diffraction pattern of the $PtSe_2$ crystals. The strong $(00n)$ peaks indicates the nice crystallization of the $PtSe_2$ crystals. The Raman spectrum of the $PtSe_2$ crystals is shown in Fig. 1(b). The E_g and A_{1g} modes at 175 and 205 cm^{-1}, respectively, of the $PtSe_2$ crystals are observed. The components of the $PtSe_2$ crystals were measured by the energy dispersive x-ray spectrometry (EDS). The EDS result in Fig. 1(c) gave a Pt:Se atomic ratio of ≈1:1.9, indicating the stoichiometric ratio of the crystals.

The thin $PtSe_2$ microcrystals were mechanically exfoliated from single crystals onto the 300-nm SiO_2/Si substrates. The hole density of $PtSe_2$ materials studied in this work is on the order of $6 \times 10^{20}\ \mathrm{cm}^{-3}$ at low temperatures (see Fig. S1 in Ref. [21]). The electrodes (10 nm Ti/100 nm Au) were well patterned onto the microflakes by standard photolithography followed by electron beam evaporation deposition and lift-off process. The thickness of microflakes were determined by atomic force microscopy (AFM). The four-probe resistance measurements were carried out on a Quantum Design

*lizhaoguo@caep.cn
†wuweidongding@163.com

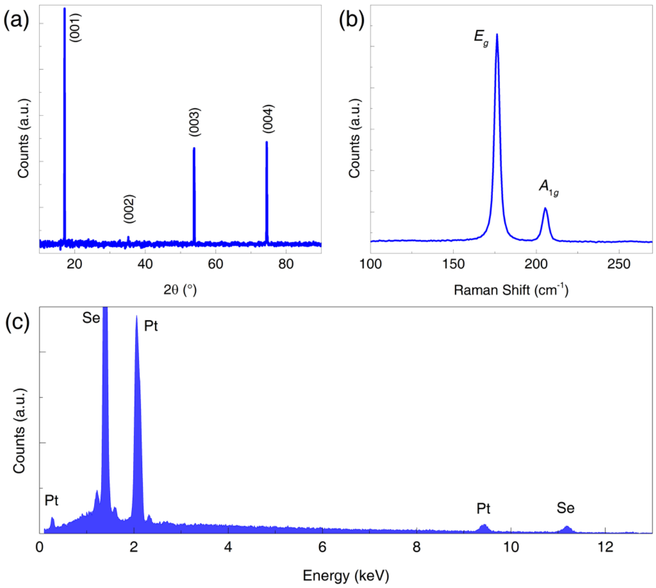

FIG. 1. The general characterizations of the $PtSe_2$ crystals. (a) The x-ray diffraction pattern of the $PtSe_2$ crystals. The strong (00n) peaks can be seen. (b) The Raman spectrum of the $PtSe_2$ crystals. The peaks at 175 and 205 cm^{-1} correspond to the E_g and A_{1g} modes of the $PtSe_2$ crystals, respectively. (c) The EDS spectrum of the $PtSe_2$ crystals, which indicates the stoichiometric ratio of the crystals.

Physical Property Measurement System, which was equipped with a vertical sample rotator. The measurement current and frequency are 50 μA and 3 Hz, respectively.

III. RESULTS

The bulk $PtSe_2$ belongs to the D_{3d}^3 space group of the centrosymmetric trigonal crystal structure, which is a periodic stack of layered basic building blocks with weak van der Waals interlayer interactions. In each layer, Pt atoms are sandwiched by a top and bottom Se layer, whereas two Se atoms are related by inversion symmetry. In this work, we define the $\boldsymbol{a}$ axis along the direction of Pt chains, and the $\boldsymbol{b}$ axis is perpendicular to $\boldsymbol{a}$ in the layer plane [the lower inset of Fig. 2(a)]. Therefore, the thin $PtSe_2$ crystals can be exfoliated by using scotch tape. The upper inset in Fig. 2(a) shows the optical image of a $PtSe_2$ thin flake, its thickness is ∼17 nm, which is determined by AFM measurement. We named this device as S1, in which the electric field $\boldsymbol{E}$ is along the $\boldsymbol{b}$ axis.

The electric transport properties of sample S1 are investigated. The temperature dependence of resistivity reveals a metallic bulk in this thin $PtSe_2$ flake [Fig. 2(a)]. Figure 2(b) shows the resistivity as a function of angle θ in several fixed fields at $T = 2$ K, where θ is defined as an angle between the magnetic field $\boldsymbol{B}$ and electric field $\boldsymbol{E}$ in the $\boldsymbol{a}$-$\boldsymbol{b}$ plane. We can see that the angular dependences of MR display strong anisotropy and twofold oscillations. The anisotropic MR may arise from the anisotropy of the Fermi surface because of the anisotropic effective mass and/or lattice scattering time in $PtSe_2$ materials [11,22,23]. In addition, the minimum of resistivity (maximum of conductivity) is achieved at $\theta = 0^\circ$ and 180°, where $\boldsymbol{B}$ aligns with $\boldsymbol{E}$.

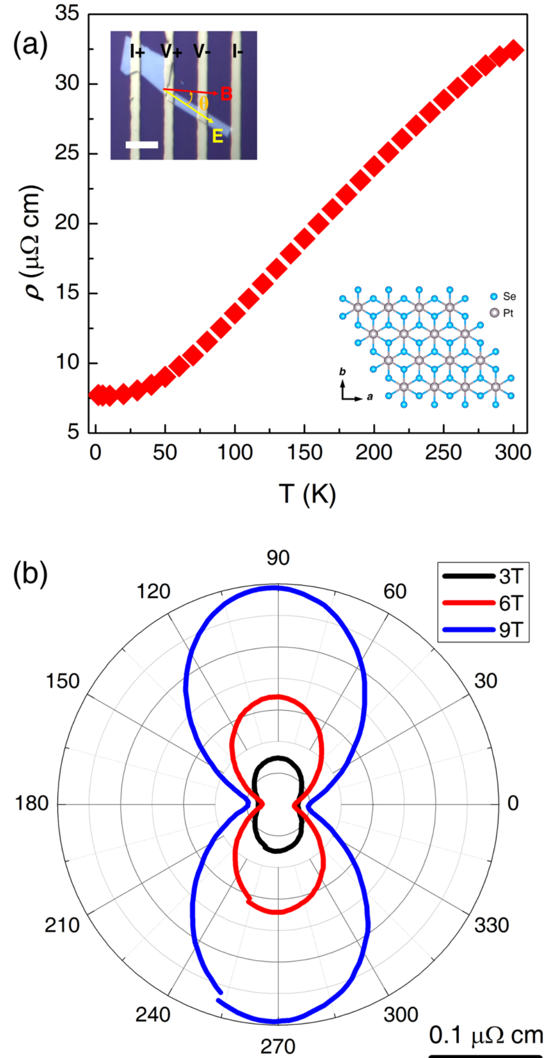

FIG. 2. Electrical resistivity of a $PtSe_2$ microflake (sample S1). (a) Temperature dependence of resistivity ρ of sample S1. The upper inset is the optical image of S1, scale bar is 10 μm. The definition of angle θ between the magnetic field $\boldsymbol{B}$ and electrical field (current) $\boldsymbol{E}$ is also shown. The lower inset shows the top view of the crystal structure of monolayer $PtSe_2$, where the $\boldsymbol{a}$ and $\boldsymbol{b}$ axes are defined. (b) The polar representation of ρ vs θ at fixed fields as indicated, at $T = 2$ K. The minimum magnetoresistivity values are found at $\theta = 0^\circ$ and 180°, which is $\boldsymbol{B} \| \boldsymbol{E}$.

Then, we performed the MR measurements on the sample S1 by applying a magnetic field parallel to the current direction ($\boldsymbol{B} \| \boldsymbol{E}$). Figure 3(a) presents the MR curve with $\theta = 0^\circ$ at $T = 2$ K, the notable negative longitudinal MR in $PtSe_2$ microflakes is demonstrated in an intermediate field range (region II). At the weak field regime (region I: $|B| \lesssim 1$ T), a resistivity dip around zero field was observed, which could be ascribed to the weak antilocalization (WAL) effect due to the spin-orbit coupling in $PtSe_2$ [24]. At the high field regime (region III: $B \gtrsim 6$ T), a positive MR signal was obtained. Its physical mechanism remains unclear, and will be discussed below. Figure 3(b) displays the longitudinal MR curves at various temperatures. One can see that the negative MR arrived with the maximum (−1‰) at $T = 2$ K

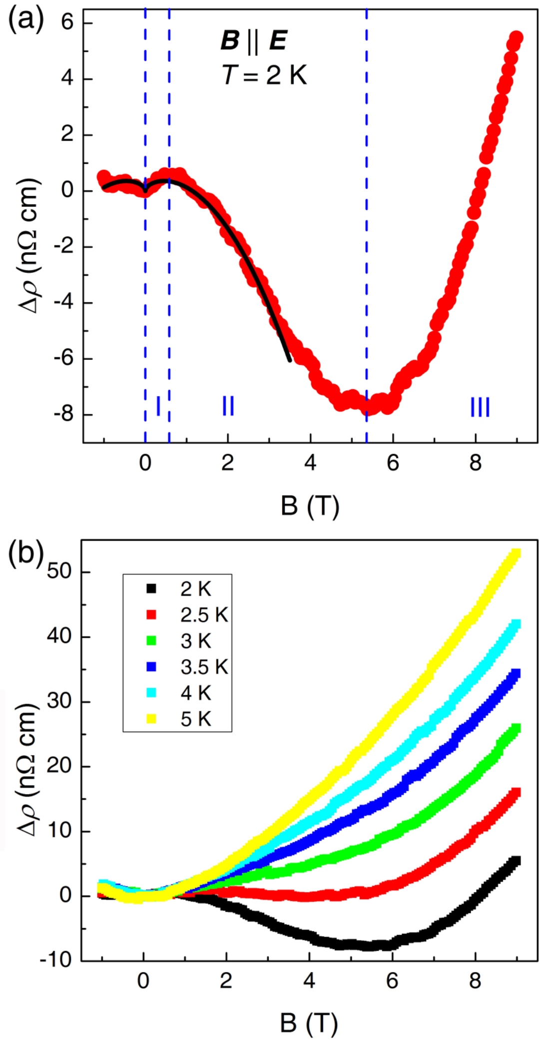

FIG. 3. Negative longitudinal magnetoresistance (MR) of a $PtSe_2$ microflake (sample S1) with the $\boldsymbol{B}\|\boldsymbol{E}$ condition. (a) The longitudinal MR curve at $T = 2\,\mathrm{K}$ with $\boldsymbol{B}\|\boldsymbol{E}$ condition, where $\Delta\rho = \rho(B)–\rho(B=0)$. The solid curve is the Adler-Bell-Jackiw (ABJ) theoretical fitting result. The MR curve can be divided into three regions, which are labeled as I–III. The region I represents the WAL effect, the region II characterizes the ABJ negative MR component, and region III contains the positive longitudinal MR component. (b) The longitudinal MR curves at various temperatures with $\boldsymbol{B}\|\boldsymbol{E}$ condition. The negative MR is apparently suppressed at ~3 K.

and rapidly vanished while temperature was above a threshold value ($T \gtrsim 3$ K). The symmetric longitudinal MR curve of S1 is obtained while sweeping the magnetic field from −9 to 9 T [see below, Fig. 5(a)]. This result signifies that the negative longitudinal MR is the intrinsic property of $PtSe_2$ microflakes, rather than from the sample geometry effect of electrical measurements.

Next, we measured the MR curves of S1 at various θ at $T = 2\,\mathrm{K}$, as shown in Figs. 4(a)–4(c). We can see that the negative longitudinal MR exhibits the strongest signal at $\theta = 0^\circ$, while at $\theta \gtrsim 30^\circ$, the negative MR is completely suppressed, and the strongest positive MR reaches up to ~2.4% when magnetic field is perpendicular to the current. The similar magnetotransport features are also observed in Weyl [25,26] and Dirac [27,28] semimetals.

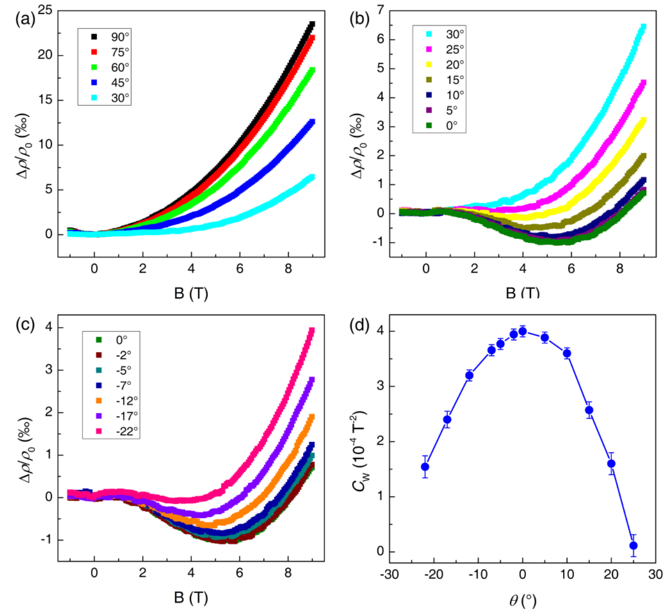

FIG. 4. Angular dependence of negative magnetoresistance of a $PtSe_2$ microflake (sample S1). The longitudinal MR curves in the angle θ ranges of (a) $90^\circ \sim 30^\circ$, (b) $30^\circ \sim 0^\circ$, and (c) $0^\circ \sim -22^\circ$, at $T = 2\,\mathrm{K}$, where $\Delta\rho/\rho_0(‰) = [\rho(B)–\rho(B=0)]/\rho(B=0) \times 1000‰$. The apparently suppressed negative MR at $|\theta| \gtrsim 25^\circ$ can be seen. (d) The angular dependence of the chiral anomaly coefficient C_W, which is extracted from the semiclassical fittings of experimental data. The results show the strong angle θ sensitivity of C_W.

The negative longitudinal MR is also sensitive to the Fermi level of $PtSe_2$ flake. Figure 5(a) shows the longitudinal MR curves of sample S1 at different measurement times; one is obtained for the as-prepared sample and another is measured 8 months later from the first measurement. We can see that the negative longitudinal MR is observed both in the two measurements. However, the negative MR value, measured eight months later, is weakened comparing to the first measurement. The reason may be ascribed to the Fermi level far away from the Dirac point due to the electron doping from air [29]. The Fermi level can be further tuned by the back gate voltage (V_G). Figure 5(b) presents the longitudinal MR curves at various V_G from −50 to +50 V. The notable negative longitudinal MR was observed at $V_G = –50\,\mathrm{V}$, it was gradually suppressed as V_G increased and completely disappeared at $V_G = 50\,\mathrm{V}$. The gate-tunable negative longitudinal MR effect implies that as V_G increases, the Fermi level moves away from the Dirac points from above. This result suggests that the negative longitudinal MR in $PtSe_2$ microflakes can be altered by gate voltage in a controllable way. As we know, the carrier density on the order of $10^{12} \sim 10^{13}\,\mathrm{cm}^{-2}$ can be tuned by the 300-nm-thick SiO_2 dielectric layer. It seems that the gate-tunable transport property is impossible in our $PtSe_2$ microflakes due to their high carrier density. However, the thickness-modulated metal-to-semiconductor transformation provides an opportunity to control the electrical transport by gate voltage in the ultrathin $PtSe_2$ flakes [19].

The negative longitudinal MR was further confirmed in another $PtSe_2$ microflake (sample S2). The inset of Fig. 6(a) shows the optical image of device S2, the thickness of flake S2

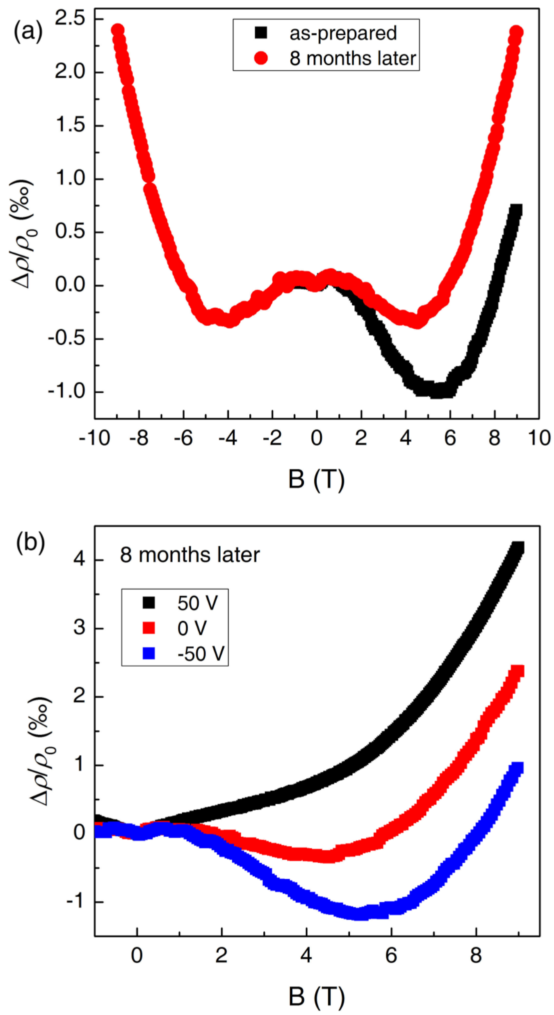

FIG. 5. Tuning the negative longitudinal magnetoresistance of a $PtSe_2$ microflakes (sample S1) by changing the Fermi level ($T = 2$ K with $\boldsymbol{B}\|\boldsymbol{E}$). (a) The measured negative longitudinal MR curves of S1 at different times. The black curve is the MR data for the first measurement (as-prepared sample), the red curve is the MR data for the second measurement (eight months from the first measurement). The symmetric MR curve can be seen while sweeping the magnetic field from negative (–9 T) to positive (9 T) fields. (b) The negative longitudinal MR of sample S1 for various gate voltages (V_G), which shows a suppressed negative longitudinal MR effect while increasing V_G from −50 V to +50 V.

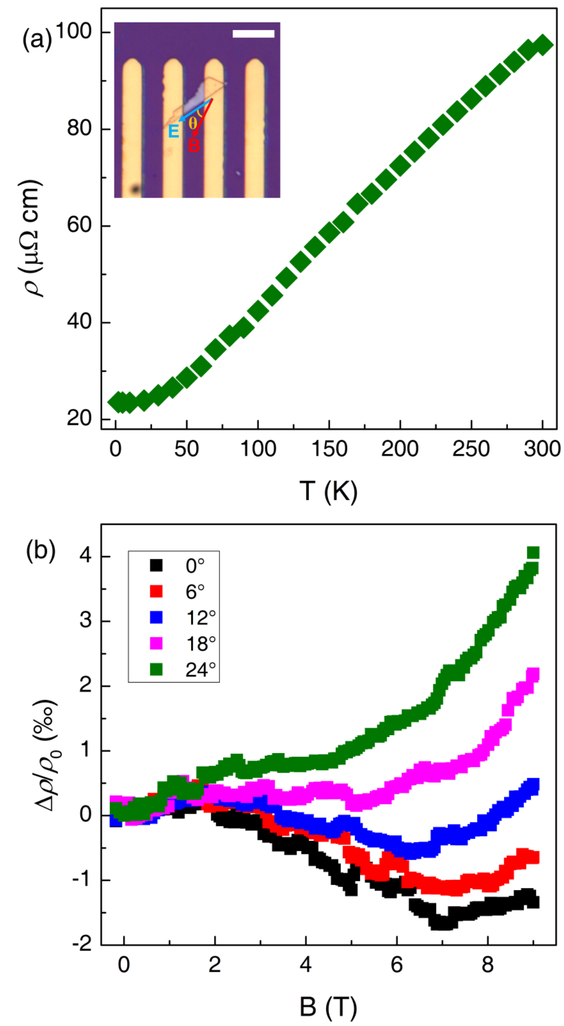

FIG. 6. Negative longitudinal magnetoresistance of another $PtSe_2$ microflakes (sample S2). (a) Temperature dependence of resistivity ρ of sample S2. The larger resistivity values of S2, compared with S1, resulted from the contact and electrode resistances in the two-probe measurements. The upper inset is its optical image, scale bar is 10 μm. The definition of angle θ between the magnetic field $\boldsymbol{B}$ and electrical field (current) $\boldsymbol{E}$ is also shown. (b) The longitudinal MR curves at various angles as indicated, at $T = 2$ K. The apparently suppressed negative MR at $|\theta| \gtrsim 24^\circ$ can be seen.

is around 10 nm. The magnetotransport properties of S2 were measured in a two-probe configuration. Figure 6(b) presents the MR curves at various angles. While $\theta = 0^\circ$ (i.e., $\boldsymbol{B}\|\boldsymbol{E}$), the strongest negative MR is observed, the maximum negative MR reaches up to −1.6‰. The critical field B_C where the MR is a crossover from negative to positive is ∼7 T for S2; this value is larger than that of sample S1. The negative MR also vanished at $\theta \gtrsim 25^\circ$.

IV. DISCUSSION

Negative MR is a novel transport phenomenon in metals. Several models have been proposed to explain this phenomenon. In this section, we attempt to explain the observed negative MR in our $PtSe_2$ microflakes. First, the weak localization (WL) effect will results a negative MR with in-plane field configuration [30,31]. However, we can rule out this mechanism because the strong WL signal (negative MR) should be observed at $\theta = 90^\circ$. Second, the negative longitudinal MR is usually observed in magnetic materials [32]. The magnetic scattering mechanism can be obviously excluded due to the absence of magnetic order in $PtSe_2$ materials. The third possible origin is the geometry or size effect of the samples, such as current jetting [33]. This mechanism is also inappropriate for our experimental results due to the temperature insensitivity of this effect. And the well-defined electrodes of our $PtSe_2$ samples could overcome the geometry effect. Fourth, the negative longitudinal MR is also expected in the case of the ultraquantum limit ($\omega\tau \gg 1$, where ω is the cyclotron frequency and τ is the transport life time) for any 3D metal, regardless of its band structure [34–36]. We have estimated that $\omega\tau \sim 1$ at the magnetic fields where negative longitudinal MR is observed, for our $PtSe_2$ microflakes. This result indicates that the samples remain in the semiclassical limit, and removes this origin. By excluding the above possible mechanisms, we speculate that the negative longitudinal MR in our $PtSe_2$ microflakes is related to the chiral anomaly of Weyl nodes. In the following, we will apply the chiral anomaly theory to our experimental results. Moreover, the nontopological origin of negative longitudinal MR is also discussed.

A. Theoretical background of chiral anomaly

The chiral anomaly effect is a remarkable phenomenon to describe the generation of an electric current induced by chirality imbalance of Weyl fermions in the presence of a magnetic field. This effect was mainly investigated in high-energy particle physics previously [37,38], and referred as the Adler-Bell-Jackiw (ABJ) effect. Weyl semimetals, which host Weyl fermions as emergent quasiparticles, provide a perfect platform to study the ABJ anomaly effect in condensed matter [1,39,40]. For a 3D Dirac semimetal, the Dirac point is composed of two overlapping Weyl nodes with opposite chirality, which can be separated in momentum space by breaking the time-reversal symmetry or the spatial inversion symmetry [41]. Therefore, the ABJ anomaly is also expected in Dirac semimetals [42,43].

The negative longitudinal MR shows significant transport evidence from the ABJ chiral anomaly in topological Weyl and Dirac semimetals [44–46]. While an external magnetic field $\boldsymbol{B}$ is applied, the Dirac point in a 3D Dirac semimetal splits into two Weyl nodes with opposite chirality along the field direction [Fig. 7(b)]. In such a case, the right- and left-handed fermions in the different Weyl nodes have equal chemical potential $\mu_R = \mu_L$. While an electric field $\boldsymbol{E}$ is also applied and parallel to the magnetic field, a population imbalance ($\mu_R \neq \mu_L$) between two Weyl nodes occurred, which induces a charge pumping from one Weyl node to another with opposite chirality [Fig. 7(c)]. The charge pumping rate between the two nodes can be described by [47]

$$W = \chi \frac{e^3}{4\pi^2\hbar^2}\boldsymbol{E}\cdot\boldsymbol{B}, \tag{1}$$

where $\chi = \pm 1$ is the chirality of the Weyl nodes, $\hbar$ is the reduced Planck's constant and e is the electron charge. This effect is referred to as the chiral anomaly, which means that the chiral charge is not conserved. The charge annihilated at one Weyl nodes will be generated at the other node with opposite chirality, and thus the charge is conserved in the whole system. However, the opposite process (that is, the chiral charge is transferred from the high potential to the low potential) always exists and is characterized by a relaxation time τ_a. Finally, a charge balance between the pumping and relaxation processes is established, and a net current is generated in the

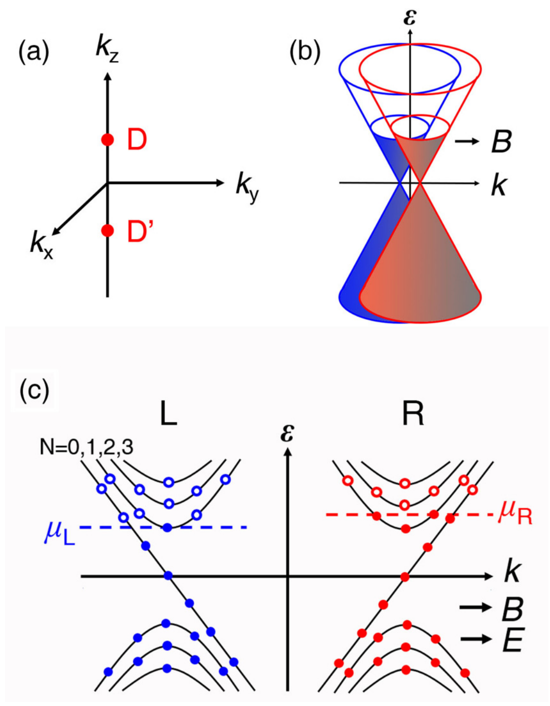

FIG. 7. Illustration of chiral anomaly in Dirac semimetal. (a) Sketch of Dirac points at D and D' along the k_z axis in the Brillouin zone of $PtSe_2$. (b) A Dirac cone is separated into two Weyl cones with opposite chirality (right handed or left handed) along with the direction of magnetic field $\boldsymbol{B}$. (c) Cartoon of the chiral anomaly of Weyl nodes in the $\boldsymbol{B}\|\boldsymbol{E}$ configuration. L and R represent the left-handed and right-handed Weyl nodes respectively. A magnetic field $\boldsymbol{B}$ parallel to the electric field $\boldsymbol{E}$ generates an imbalance of chiral charges between the two opposite Weyl nodes resulting in a negative longitudinal magnetoresistance.

direction of the electric field. Therefore, a negative MR will be induced. Since the chiral charge pumping occurred when $\boldsymbol{B}\cdot\boldsymbol{E} \neq 0$ [Eq. (1)], one expected that the ABJ anomaly induced negative MR is sensitive to the angle between $\boldsymbol{B}$ and $\boldsymbol{E}$ [48]. Quantitatively, under the semiclassical approximation, in the case of $\boldsymbol{B}\|\boldsymbol{E}$ and zero temperature, the anomaly conductivity can be expressed as [44,49,50]

$$\sigma = \frac{e^4 v_F^3 B^2 \tau_a}{4\pi^2\hbar\epsilon_F^2}, \tag{2}$$

where v_F is the Fermi velocity near the Weyl node, τ_a is the intervalley scattering time, and ϵ_F is the measured chemical potential from the energy of the Dirac point. The quadratic law of conductivity leading to a negative MR has been widely observed in 3D topological insulators [51–53], the topological Weyl (TaAs [26,54], WTe_2 [25,55–57], TaP [58–60], NbP [61,62], NbAs [63,64], β-Ag_2Se [65], $Y_2Ir_2O_7$ [66], $Co_3Sn_2S_2$ [67], etc.) and Dirac (Na_3Bi [68,69], $ZrTe_5$ [70–73], Cd_3As_2 [27,28,74–79], $HfTe_5$ [80], NdSb [81], $SrAs_3$ [82], etc.) semimetals [83,84], and some zero-gap semimetals [85–87].

B. Chiral anomaly in $PtSe_2$ microflakes

To qualitatively describe the negative longitudinal MR in $PtSe_2$ microflakes. We use the semiclassical magnetoconductance formula that includes the contribution from the ABJ chiral anomaly and WAL effect [51]:

$$\sigma(B) = \sigma_{\rm N} + (1 + C_{\rm W} B_{\parallel}^2) \cdot \sigma_{\rm WAL}, \tag{3a}$$

$$\sigma_{\rm N}(B) \simeq \frac{\sigma_{\rm N0}}{1 + C_{\rm N} B^2}\,, \tag{3b}$$

$$\sigma_{\rm WAL}(B) \simeq \sigma_{\rm WAL0} + C_{\rm WAL} \cdot \sqrt{B}, \tag{3c}$$

where $\sigma_{\rm N}$ is the conventional MR which comes from Fermi surface contributions except for Weyl nodes. $\sigma_{\rm WAL}$ is the WAL conductivity from quantum interference corrections associated with spin-orbit scattering. The term of $C_{\rm W} B_{\parallel}^2$ in Eq. (3a) is due to the ABJ chiral anomaly [Eq. (2)], $C_{\rm W}$ is the chiral coefficient, and $B_{||} = B \cos\theta$ is the magnetic field component along the electric field. $\sigma_{\rm N0}$, $C_{\rm N}$ and $\sigma_{\rm WAL0}$, $C_{\rm WAL}$ are positive coefficients to describe the contribution of normal and WAL MR, respectively. A typical fitting result is shown in Fig. 3(a) by the solid curve. We can see that the Eq. (3) perfectly describes the MR data at the low fields region (region I and II), which includes the negative longitudinal MR. We applied Eq. (3) to the MR curves at various angles. The extracted $C_{\rm W}$ as a function of θ are displayed in Fig. 4(d). It can be seen that $C_{\rm W}$ reaches maximum at $\theta = 0^\circ$. This result further confirms the strongly angle sensitivity of the ABJ chiral anomaly. Because the $C_{\rm W}$ is sensitive to the Fermi level [Eq. (2)], we therefore observed a gate-tunable negative longitudinal MR in our $PtSe_2$ microflakes [Fig. 5(b)].

The negative longitudinal MR as evidence of ABJ chiral anomaly, which was observed in our thin $PtSe_2$ microflakes, is induced by the type-I Weyl nodes despite $PtSe_2$ being identified as a type-II Dirac semimetal. The first-principles calculations predicted that a pair of Dirac points is located at the D and D′ points along the k_z direction [8] [Fig. 7(a)]. The Dirac cone is strongly tilted along the k_z direction which can be regarded as the type-II Dirac fermions, and the conventional Dirac cones are found in the k_x and k_y directions. Therefore, the chiral anomaly of type-II Weyl nodes in $PtSe_2$ should emerge, while $\boldsymbol{B} \parallel \boldsymbol{E} \parallel \boldsymbol{c}$, and the observed negative MR in our experiments with $\boldsymbol{B} \parallel \boldsymbol{E} \parallel \boldsymbol{b}$ condition originates from the type-I Weyl nodes, analogous to the observations in Na_3Bi [68] and Cd_3As_2 [27,28,75].

The negative longitudinal MR of $PtSe_2$ microflakes is sensitive to the thickness as well. Figure S2 [21] shows the longitudinal MR curves of two thick $PtSe_2$ microflakes (their thicknesses are 42 and 95 nm, respectively) at $T = 2\,{\rm K}$ and $\boldsymbol{B} \| \boldsymbol{E}$. There are no negative MR signatures that can be seen. The positive MR arrived at $\sim$4 and $\sim$1.5% at $B = 9\,{\rm T}$, and these values are several dozen times larger than those of the thin flake ($\sim$0.7‰ for S1). The completely suppressed negative longitudinal MR in the thick samples may result from the giant contribution of the positive MR. The thickness sensitivity of the chiral anomaly is observed in WTe_2 [25,56]. Therefore, this accurate mechanism deserves further investigation.

C. Nontopological origin

Recently, Andreev and Spivak [46] have shown that the negative longitudinal MR can also exist in conventional centrosymmetric and time-reversal invariant conductors in a certain range of parameters. As we know, the Dirac points in Dirac semimetals are protected only by the crystalline symmetry, an energy gap Δ can be opened at the Dirac point due to the small lattice distortion, making it nontopological. In such a case, the chirality is no longer conserved and there is no chiral anomaly. However, the helicity is conserved, and a helicity imbalance between the two nodes occurs due to the acceleration of electrons by the electric field directed along $\boldsymbol{B}$. In a conventional conductor, the large ratio of the Fermi energy $\epsilon_{\rm F}$ to the band gap Δ produces a large value of $\tau_h/\tau_{tr} = \xi\epsilon_F^2/\Delta^2$ (τ_h is the helicity relaxation time, τ_{tr} is the transport mean free time, and ξ is a numerical coefficient of the order of unity), which also leads to a B^2 negative longitudinal MR. For our $PtSe_2$ microflakes, the small residual resistivity ratio [RRR $= \rho(300\,{\rm K})/\rho(2\,{\rm K}) \sim 5$] implies that a large number of impurities and/or disorders exist in the $PtSe_2$ bulk. Then, a small gap may be opened at the Dirac point, which pushes the $PtSe_2$ metals into the nontopological regime. Furthermore, the high carrier density means that the Fermi level is far away the Dirac point. We can speculate that $\epsilon_{\rm F}/\Delta$ is very large in our $PtSe_2$ microflakes. These conditions meet the prerequisites of the Andreev-Spivak model, therefore, another possible mechanism of the observed negative longitudinal MR in our $PtSe_2$ microflakes is the nontopological effect of conventional conductors. Because the nontopological B^2 negative longitudinal MR is sensitive to $\epsilon_{\rm F}/\Delta$, we expect that the MR can be controlled by the gate voltage [Fig. 5(b)].

Up to now we have explained the negative longitudinal MR of $PtSe_2$ microflakes based on the ABJ chiral anomaly of topological semimetals and the helicity pumping effect of conventional conductors. For the topological origin, the chiral feature of Dirac fermions seems completely relaxed because the Dirac point is more than 1 eV below the Fermi energy [10]. For the nontopological origin, the small energy gap at the Dirac point should be further confirmed. Therefore, the exact physical mechanism of negative longitudinal MR in our $PtSe_2$ microflakes remains unknown and deserves further investigation.

The physical mechanism behind the large positive MR in region III [Figs. 3(a) and 6(b)] is also unclear even though some theoretical proposals could be used to explain this phenomenon. One possible origin is the classical MR of metals due to the Lorentz force. According to the traditional MR theory, the resistance is independent of the field while $\boldsymbol{B} \| \boldsymbol{E}$ owing to the absence of the Lorentz force. However, the electron diffusion directions are not always parallel to the external magnetic field direction. Due to the relevant scattering processes, this small deviation of carrier's diffusion direction from that of the field will induce a finite MR in materials. Another mechanism is the WAL effect of the normal fermions rather than the Weyl/Dirac fermions in the topological semimetals. Besides the Dirac fermions at the Fermi energy, the conventional fermions also exist and denote a WAL MR [8]. This conventional MR is becoming dominant while the chiral anomaly of Weyl nodes is suppressed.

V. CONCLUSION

To summarize, we report the experimental observations of negative longitudinal MR in thin $PtSe_2$ microflakes. This negative MR is sensitive to the angle between $\boldsymbol{B}$ and $\boldsymbol{E}$, and rapidly vanishes with temperature increasing, and can be controlled by a gate voltage. By excluding other physical mechanisms, we speculate that the observed negative longitudinal MR in $PtSe_2$ thin crystals is related to the ABJ chiral anomaly of Dirac fermions of $PtSe_2$ materials. Furthermore, the nontopological origin of the negative longitudinal MR is also discussed. Our work gives experimental evidence of the anomalous transport property in $PtSe_2$ crystals, which may be useful for any electronic applications in the future.

ACKNOWLEDGMENTS

This work is financially supported by the National Natural Science Foundation of China (Grant No. 11604310), the National Key Scientific Instrument and Equipment Development Project of China (Grant No. 2014YQ090709), and the Key Laboratory of Ultra-Precision Machining Technology Foundation of CAEP (Grant No. ZZ15003).

[1] X. Wan, A. M. Turner, A. Vishwanath, and S. Y. Savrasov, Phys. Rev. B **83**, 205101 (2011).
[2] Z. Wang, Y. Sun, X.-Q. Chen, C. Franchini, G. Xu, H. Weng, X. Dai, and Z. Fang, Phys. Rev. B **85**, 195320 (2012).
[3] A. A. Soluyanov, D. Gresch, Z. Wang, Q. Wu, M. Troyer, X. Dai, and B. A. Bernevig, Nature (London) **527**, 495 (2015).
[4] M. Udagawa and E. J. Bergholtz, Phys. Rev. Lett. **117**, 086401 (2016).
[5] T. E. O'Brien, M. Diez, and C. W. J. Beenakker, Phys. Rev. Lett. **116**, 236401 (2016).
[6] Z.-M. Yu, Y. Yao, and S. A. Yang, Phys. Rev. Lett. **117**, 077202 (2016).
[7] S. Tchoumakov, M. Civelli, and M. O. Goerbig, Phys. Rev. Lett. **117**, 086402 (2016).
[8] H. Huang, S. Zhou, and W. Duan, Phys. Rev. B **94**, 121117 (2016).
[9] K. Zhang, M. Yan, H. Zhang, H. Huang, M. Arita, Z. Sun, W. Duan, Y. Wu, and S. Zhou, Phys. Rev. B **96**, 125102 (2017).
[10] Y. Li, Y. Xia, S. A. Ekahana, N. Kumar, J. Jiang, L. Yang, C. Chen, C. Liu, B. Yan, C. Felser, G. Li, Z. Liu, and Y. Chen, Phys. Rev. Mater. **1**, 074202 (2017).
[11] Z. Li, J. Zhang, Y. Zeng, L. Meng, M. Zhou, and W. Wu, J. Phys.: Condens. Matter **29**, 23LT01 (2017).
[12] C. Yim, V. Passi, M. C. Lemme, G. S. Duesberg, C. O. Coileain, E. Pallecchi, D. Fadil, and N. McEvoy, npj 2D Mater. Appl. **2**, 5 (2018).
[13] H. Yang, M. Schmidt, V. Suss, M. Chan, F. F. Balakirev, R. D. McDonald, S. S. P. Parkin, C. Felser, B. Yan, and P. J. W. Moll, New J. Phys. **20**, 043008 (2018).
[14] Y. Wang, L. Li, W. Yao, S. Song, J. T. Sun, J. Pan, X. Ren, C. Li, E. Okunishi, Y.-Q. Wang, E. Wang, Y. Shao, Y. Y. Zhang, H.-t. Yang, E. F. Schwier, H. Iwasawa, K. Shimada, M. Taniguchi, Z. Cheng, S. Zhou, S. Du, S. J. Pennycook, S. T. Pantelides, and H.-J. Gao, Nano Lett. **15**, 4013 (2015).
[15] Z. Wang, Q. Li, F. Besenbacher, and M. Dong, Adv. Mater. **28**, 10224 (2016).
[16] Y. Zhao, J. Qiao, Z. Yu, P. Yu, K. Xu, S. P. Lau, W. Zhou, Z. Liu, X. Wang, W. Ji, and Y. Chai, Adv. Mater. **29**, 1604230 (2017).
[17] C. Yim, K. Lee, N. McEvoy, M. O'Brien, S. Riazimehr, N. C. Berner, C. P. Cullen, J. Kotakoski, J. C. Meyer, M. C. Lemme, and G. S. Duesberg, ACS Nano **10**, 9550 (2016).
[18] X. Yu, P. Yu, D. Wu, B. Singh, Q. Zeng, H. Lin, W. Zhou, J. Lin, K. Suenaga, Z. Liu, and Q. J. Wang, Nat. Commun. **9**, 1545 (2018).
[19] A. Ciarrocchi, A. Avsar, D. Ovchinnikov, and A. Kis, Nat. Commun. **9**, 919 (2018).
[20] Z. Li, Y. Zeng, M. Zhou, B. Xie, J. Zhang, and W. Wu, Nanotechnology **29**, 40LT01 (2018).
[21] See Supplemental Material at http://link.aps.org/supplemental/10.1103/PhysRevB.98.165441 for additional transport properties in the thick microflakes.
[22] L. R. Thoutam, Y. L. Wang, Z. L. Xiao, S. Das, A. Luican-Mayer, R. Divan, G. W. Crabtree, and W. K. Kwok, Phys. Rev. Lett. **115**, 046602 (2015).
[23] A. Collaudin, B. Fauque, Y. Fuseya, W. Kang, and K. Behnia, Phys. Rev. X **5**, 021022 (2015).
[24] W. Yao, E. Wang, H. Huang, K. Deng, M. Yan, K. Zhang, K. Miyamoto, T. Okuda, L. Li, Y. Wang, H. Gao, C. Liu, W. Duan, and S. Zhou, Nat. Commun. **8**, 14216 (2017).
[25] Y. Wang, E. Liu, H. Liu, Y. Pan, L. Zhang, J. Zeng, Y. Fu, M. Wang, K. Xu, Z. Huang, Z. Wang, H.-Z. Lu, D. Xing, B. Wang, X. Wan, and F. Miao, Nat. Commun. **7**, 13142 (2016).
[26] X. Huang, L. Zhao, Y. Long, P. Wang, D. Chen, Z. Yang, H. Liang, M. Xue, H. Weng, Z. Fang, X. Dai, and G. Chen, Phys. Rev. X **5**, 031023 (2015).
[27] C.-Z. Li, L.-X. Wang, H. Liu, J. Wang, Z.-M. Liao, and D.-P. Yu, Nat. Commun. **6**, 10137 (2015).
[28] H. Li, H. He, H.-Z. Lu, H. Zhang, H. Liu, R. Ma, Z. Fan, S.-Q. Shen, and J. Wang, Nat. Commun. **7**, 10301 (2016).
[29] Z. G. Li, I. Garate, J. Pan, X. G. Wan, T. S. Chen, W. Ning, X. O. Zhang, F. Q. Song, Y. Z. Meng, X. C. Hong, X. F. Wang, L. Pi, X. R. Wang, B. G. Wang, S. Y. Li, M. A. Reed, L. Glazman, and G. H. Wang, Phys. Rev. B **91**, 041401 (2015).
[30] C. W. J. Beenakker and H. van Houten, Phys. Rev. B **38**, 3232 (1988).
[31] C. J. Lin, X. Y. He, J. Liao, X. X. Wang, V. Sacksteder, W. M. Yang, T. Guan, Q. M. Zhang, L. Gu, G. Y. Zhang, C. G. Zeng, X. Dai, K. H. Wu, and Y. Q. Li, Phys. Rev. B **88**, 041307 (2013).
[32] L. Ritchie, G. Xiao, Y. Ji, T. Y. Chen, C. L. Chien, M. Zhang, J. Chen, Z. Liu, G. Wu, and X. X. Zhang, Phys. Rev. B **68**, 104430 (2003).
[33] J. Hu, T. F. Rosenbaum, and J. B. Betts, Phys. Rev. Lett. **95**, 186603 (2005).
[34] P. N. Argyres and E. N. Adams, Phys. Rev. **104**, 900 (1956).
[35] P. Goswami, J. H. Pixley, and S. Das Sarma, Phys. Rev. B **92**, 075205 (2015).
[36] B. A. Assaf, T. Phuphachong, E. Kampert, V. V. Volobuev, P. S. Mandal, J. Sánchez-Barriga, O. Rader, G. Bauer, G. Springholz,

L. A. de Vaulchier, and Y. Guldner, Phys. Rev. Lett. **119**, 106602 (2017).
[37] S. L. Adler, Phys. Rev. **177**, 2426 (1969).
[38] J. S. Bell and R. Jackiw, Nuovo Cimento A **60**, 47 (1969).
[39] H. B. Nielsen and M. Ninomiya, Phys. Lett. B **130**, 389 (1983).
[40] V. Aji, Phys. Rev. B **85**, 241101 (2012).
[41] S. M. Young, S. Zaheer, J. C. Y. Teo, C. L. Kane, E. J. Mele, and A. M. Rappe, Phys. Rev. Lett. **108**, 140405 (2012).
[42] A. A. Burkov, Phys. Rev. B **91**, 245157 (2015).
[43] N. P. Armitage, E. J. Mele, and A. Vishwanath, Rev. Mod. Phys. **90**, 015001 (2018).
[44] D. T. Son and B. Z. Spivak, Phys. Rev. B **88**, 104412 (2013).
[45] A. A. Burkov, Phys. Rev. Lett. **113**, 247203 (2014).
[46] A. V. Andreev and B. Z. Spivak, Phys. Rev. Lett. **120**, 026601 (2018).
[47] P. Hosur and X. Qi, C. R. Physique **14**, 857 (2013).
[48] J. Behrends and J. H. Bardarson, Phys. Rev. B **96**, 060201 (2017).
[49] V. A. Zyuzin, Phys. Rev. B **95**, 245128 (2017).
[50] G. Sharma, P. Goswami, and S. Tewari, Phys. Rev. B **96**, 045112 (2017).
[51] H.-J. Kim, K.-S. Kim, J.-F. Wang, M. Sasaki, N. Satoh, A. Ohnishi, M. Kitaura, M. Yang, and L. Li, Phys. Rev. Lett. **111**, 246603 (2013).
[52] S. Wiedmann, A. Jost, B. Fauqué, J. van Dijk, M. J. Meijer, T. Khouri, S. Pezzini, S. Grauer, S. Schreyeck, C. Brüne, H. Buhmann, L. W. Molenkamp, and N. E. Hussey, Phys. Rev. B **94**, 081302(R) (2016).
[53] D. Shin, Y. Lee, M. Sasaki, Y. H. Jeong, F. Weickert, J. B. Betts, H.-J. Kim, K.-S. Kim, and J. Kim, Nat. Mater. **16**, 1096 (2017).
[54] C.-L. Zhang, S.-Y. Xu, I. Belopolski, Z. Yuan, Z. Lin, B. Tong, G. Bian, N. Alidoust, C.-C. Lee, S.-M. Huang, T.-R. Chang, G. Chang, C.-H. Hsu, H.-T. Jeng, M. Neupane, D. S. Sanchez, H. Zheng, J. Wang, H. Lin, C. Zhang, H.-Z. Lu, S.-Q. Shen, T. Neupert, M. Z. Hasan, and S. Jia, Nat. Commun. **7**, 10735 (2016).
[55] Y.-Y. Lv, X. Li, B.-B. Zhang, W. Y. Deng, S.-H. Yao, Y. B. Chen, J. Zhou, S.-T. Zhang, M.-H. Lu, L. Zhang, M. Tian, L. Sheng, and Y.-F. Chen, Phys. Rev. Lett. **118**, 096603 (2017).
[56] E. Zhang, R. Chen, C. Huang, J. Yu, K. Zhang, W. Wang, S. Liu, J. Ling, X. Wan, H.-Z. Lu, and F. Xiu, Nano Lett. **17**, 878 (2017).
[57] P. Li, Y. Wen, X. He, Q. Zhang, C. Xia, Z.-M. Yu, S. A. Yang, Z. Zhu, H. N. Alshareef, and X.-X. Zhang, Nat. Commun. **8**, 2150 (2017).
[58] F. Arnold, C. Shekhar, S.-C. Wu, Y. Sun, R. D. d. Reis, N. Kumar, M. Naumann, M. O. Ajeesh, M. Schmidt, A. G. Grushin, J. H. Bardarson, M. Baenitz, D. Sokolov, H. Borrmann, M. Nicklas, C. Felser, E. Hassinger, and B. Yan, Nat. Commun. **7**, 11615 (2016).
[59] J. Du, H. Wang, Q. Chen, Q. Mao, R. Khan, B. Xu, Y. Zhou, Y. Zhang, J. Yang, B. Chen, C. Feng, and M. Fang, Sci. China-Phys. Mech. Astron. **59**, 657406 (2016).
[60] J. Hu, J. Y. Liu, D. Graf, S. M. A. Radmanesh, D. J. Adams, A. Chuang, Y. Wang, I. Chiorescu, J. Wei, L. Spinu, and Z. Q. Mao, Sci. Rep. **6**, 18674 (2016).
[61] A. C. Niemann, J. Gooth, S.-C. Wu, S. Bäßler, P. Sergelius, R. Hühne, B. Rellinghaus, C. Shekhar, V. Süß, M. Schmidt, C. Felser, B. Yan, and K. Nielsch, Sci. Rep. **7**, 43394 (2017).
[62] Z. Wang, Y. Zheng, Z. Shen, Y. Lu, H. Fang, F. Sheng, Y. Zhou, X. Yang, Y. Li, C. Feng, and Z.-A. Xu, Phys. Rev. B **93**, 121112 (2016).
[63] B. Shen, X. Deng, G. Kotliar, and N. Ni, Phys. Rev. B **93**, 195119 (2016).
[64] Y. Li, Z. Wang, P. Li, X. Yang, Z. Shen, F. Sheng, X. Li, Y. Lu, Y. Zheng, and Z.-A. Xu, Front. Phys. **12**, 127205 (2017).
[65] C.-L. Zhang, F. Schindler, H. Liu, T.-R. Chang, S.-Y. Xu, G. Chang, W. Hua, H. Jiang, Z. Yuan, J. Sun, H.-T. Jeng, H.-Z. Lu, H. Lin, M. Z. Hasan, X. C. Xie, T. Neupert, and S. Jia, Phys. Rev. B **96**, 165148 (2017).
[66] A. Juyal, A. Agarwal, and S. Mukhopadhyay, Phys. Rev. Lett. **120**, 096801 (2018).
[67] E. Liu, Y. Sun, N. Kumar, L. Muechler, A. Sun, L. Jiao, S.-Y. Yang, D. Liu, A. Liang, Q. Xu, J. Kroder, V. Süß, H. Borrmann, C. Shekhar, Z. Wang, C. Xi, W. Wang, W. Schnelle, S. Wirth, Y. Chen, S. T. B. Goennenwein, and C. Felser, Nat. Phys. **14**, (2018).
[68] J. Xiong, S. K. Kushwaha, T. Liang, J. W. Krizan, M. Hirschberger, W. Wang, R. J. Cava, and N. P. Ong, Science **350**, 413 (2015).
[69] S. Liang, J. Lin, S. Kushwaha, J. Xing, N. Ni, R. J. Cava, and N. P. Ong, Phys. Rev. X **8**, 031002 (2018).
[70] Q. Li, D. E. Kharzeev, C. Zhang, Y. Huang, I. Pletikosic, A. V. Fedorov, R. D. Zhong, J. A. Schneeloch, G. D. Gu, and T. Valla, Nat. Phys. **12**, 550 (2016).
[71] G. Zheng, J. Lu, X. Zhu, W. Ning, Y. Han, H. Zhang, J. Zhang, C. Xi, J. Yang, H. Du, K. Yang, Y. Zhang, and M. Tian, Phys. Rev. B **93**, 115414 (2016).
[72] A. Pariari and P. Mandal, Sci. Rep. **7**, 40327 (2017).
[73] T. Liang, J. Lin, Q. Gibson, S. Kushwaha, M. Liu, W. Wang, H. Xiong, J. A. Sobota, M. Hashimoto, P. S. Kirchmann, Z.-X. Shen, R. J. Cava, and N. P. Ong, Nat. Phys. **14**, 451 (2018).
[74] Z. Jia, C. Li, X. Li, J. Shi, Z. Liao, D. Yu, and X. Wu, Nat. Commun. **7**, 13013 (2016).
[75] C. Zhang, E. Zhang, W. Wang, Y. Liu, Z.-G. Chen, S. Lu, S. Liang, J. Cao, X. Yuan, L. Tang, Q. Li, C. Zhou, T. Gu, Y. Wu, J. Zou, and F. Xiu, Nat. Commun. **8**, 13741 (2017).
[76] P. J. W. Moll, N. L. Nair, T. Helm, A. C. Potter, I. Kimchi, A. Vishwanath, and J. G. Analytis, Nature (London) **535**, 266 (2016).
[77] M. Wu, G. Zheng, W. Chu, W. Gao, H. Zhang, J. Lu, Y. Han, J. Yang, H. Du, W. Ning, Y. Zhang, and M. Tian, Phys. Rev. B **98**, 161110 (2018)..
[78] H. Li, H.-W. Wang, H. He, J. Wang, and S.-Q. Shen, Phys. Rev. B **97**, 201110(R) (2018).
[79] S. Nishihaya, M. Uchida, Y. Nakazawa, K. Akiba, M. Kriener, Y. Kozuka, A. Miyake, Y. Taguchi, M. Tokunaga, and M. Kawasaki, Phys. Rev. B **97**, 245103 (2018).
[80] H. Wang, C.-K. Li, H. Liu, J. Yan, J. Wang, J. Liu, Z. Lin, Y. Li, Y. Wang, L. Li, D. Mandrus, X. C. Xie, J. Feng, and J. Wang, Phys. Rev. B **93**, 165127 (2016).
[81] Y. Wang, J. H. Yu, Y. Q. Wang, C. Y. Xi, L. S. Ling, S. L. Zhang, J. R. Wang, Y. M. Xiong, T. Han, H. Han, J. Yang, J. Gong, L. Luo, W. Tong, L. Zhang, Z. Qu, Y. Y. Han, W. K. Zhu, L. Pi, X. G. Wan, C. Zhang, and Y. Zhang, Phys. Rev. B **97**, 115133 (2018).
[82] S. Li, Z. Guo, D. Fu, X.-C. Pan, J. Wang, K. Ran, S. Bao, Z. Ma, Z. Cai, R. Wang, R. Yu, J. Sun, F. Song, and J. Wen, Sci. Bull. **63**, 535 (2018).

[83] X.-T. Xu and S. Jia, Chin. Phys. B **25**, 117204 (2016).

[84] S. Jia, S.-Y. Xu, and M. Z. Hasan, Nat. Mater. **15**, 1140 (2016).

[85] M. Hirschberger, S. Kushwaha, Z. Wang, Q. Gibson, S. Liang, C. A. Belvin, B. A. Bernevig, R. J. Cava, and N. P. Ong, Nat. Mater. **15**, 1161 (2016).

[86] N. Kikugawa, P. Goswami, A. Kiswandhi, E. S. Choi, D. Graf, R. E. Baumbach, J. S. Brook, K. Sugii, Y. Iida, M. Nishio, S. Uji, T. Terashima, P. M. C. Rourke, N. E. Hussey, H. Takatsu, S. Yonezawa, Y. Maeno, and L. Balicas, Nat. Commun. **7**, 10903 (2016).

[87] J. B. He, D. Chen, W. L. Zhu, S. Zhang, L. X. Zhao, Z. A. Ren, and G. F. Chen, Phys. Rev. B **95**, 195165 (2017).